Biomaterials Science

ROYAL SOCIETY OF CHEMISTRY

PAPER

View Article Online
View Journal

Cite this: DOI: 10.1039/d4bm00379a

Self-evolving persistent luminescence nanoprobes for autofluorescence-free ratiometric imaging and on-demand enhanced chemodynamic therapy of pulmonary metastatic tumors†

Xu Zhao, *[a,b,c] Tian-Yue Gu,[a,b,c] You-Peng Xia,[a,b,c] Xue-Mei Gao,[d] Li-Jian Chen,[a,b,c] Li-Xia Yan[a,b,c] and Xiu-Ping Yan[a,b,c,d]

Precise imaging-guided therapy of a pulmonary metastasis tumor is of great significance for tumor management and prognosis. Persistent luminescence nanoparticles (PLNPs) are promising probes due to their *in situ* excitation-free and low-background imaging characteristics. However, most of the PLNP-based probes cannot intelligently distinguish between normal and tumor tissues or balance the needs of targeted accumulation and rapid metabolism, resulting in false positive signals and potential side effects. Besides, the luminescence intensity of single-emissive PLNPs is affected by external factors. Herein, we report a self-evolving double-emissive PLNP-based nanoprobe ZGMC@ZGC-TAT for pulmonary metastatic tumor imaging and therapy. Acid-degradable green-emitting PLNPs (ZGMC) with good afterglow performance and therapeutic potential are synthesized by systematic optimization of dopants. Ultra-small red-emitting PLNPs (ZGC) are then prepared as imaging and reference probes. The two PLNPs are finally covalently coupled and further modified with a cell-penetrating peptide (TAT) to obtain ZGMC@ZGC-TAT. Dual emission ensures a stable luminescence ratio (I_{700}/I_{537}) independent of probe concentration, test voltage and time gate. ZGMC degrades and phosphorescence disappears in a tumor microenvironment (TME), resulting in an increase in I_{700}/I_{537}, thus enabling tumor-specific ratiometric imaging. Cu^{2+} and Mn^{2+} released by ZGMC degradation achieve GSH depletion and enhance CDT, effectively inhibiting tumor cell proliferation. Meanwhile, the size of ZGMC@ZGC-TAT decreases sharply, and the resulting ZGC-TAT further causes nuclear pyknosis and quickly clear metabolism. The developed ZGMC@ZGC-TAT turns non-targeted lung aggregation of nanomaterials into a unique advantage, and integrates TME-triggered phosphorescence and size self-evolution, and on-demand therapeutic functions, showing outstanding prospects in precise imaging and efficient treatment of pulmonary metastatic tumors.

Received 14th March 2024,
Accepted 2nd May 2024

DOI: 10.1039/d4bm00379a

rsc.li/biomaterials-science

Introduction

Metastasis is the result of the spread of tumor cells to foreign organs and stands as a primary contributor to the high lethality of cancer.[1–4] Lungs are one of the organs most susceptible to colonization by cancer cells, given their integral role in the circulatory metabolic system.[5,6] Lung cancer exhibits the highest mortality rate nationwide, and the majority (44%) of lung cancer patients are diagnosed with metastatic disease with a five-year relative survival rate of only 8%.[7] Early diagnosis and specific treatment of lung cancer are the key to improving the survival rate of patients.[8] Therefore, it is of great significance to develop precise theranostic strategies for accurate imaging and efficient treatment of lung cancer.

Optical imaging emerges as a promising avenue in the field of precise diagnosis of tumors, with attributes such as its high sensitivity, non-toxicity, and rapid response.[9,10] However, conventional optical probes rely on continuous excitation from an external light source, which cannot avoid the problems of tissue autofluorescence interference and photobleaching of probes.[11] Persistent luminescence nanoparticles (PLNPs) with reproducible afterglow properties present great potential for low-background imaging *in vivo*.[12,13] Unfortunately,

[a]State Key Laboratory of Food Science and Technology, Jiangnan University, Wuxi 214122, China. E-mail: zhaoxu2017@jiangnan.edu.cn
[b]International Joint Laboratory on Food Safety, Jiangnan University, Wuxi 214122, China
[c]Institute of Analytical Food Safety, School of Food Science and Technology, Jiangnan University, Wuxi 214122, China
[d]Key Laboratory of Synthetic and Biological Colloids, Ministry of Education, School of Chemical and Material Engineering, Jiangnan University, Wuxi, 214122, China

†Electronic supplementary information (ESI) available: Chemicals and materials, instrumentation, synthetic procedures, experimental details and supplementary figures and table. See DOI: https://doi.org/10.1039/d4bm00379a

conventional single-emissive PLNPs are prone to produce inaccurate results because their luminescence intensity is susceptible to exogenous factors such as probe concentration, instrumental conditions, and time gating.[14,15] Our previous work has demonstrated that ratiometric phosphorescence sensors based on dual-emissive PLNPs can achieve self-calibrated readings and low background imaging, effectively circumventing the interference of the aforementioned exogenous factors. However, the developed sensors still have drawbacks such as a constant phosphorescence ratio signal in diseased and normal tissues and the inability to avoid false-positive signals caused by untargeted aggregation of nanoparticles in reticuloendothelial systems (RESs), such as the lungs.[16] Thus, the development of tumor microenvironment (TME)-responsive phosphorescence ratiometric nanoprobes is of great value in promoting the precise imaging of lung cancer.

The retention of nanoparticles at the lesion site affects their imaging and therapeutic efficacy, and the size of nanoparticles is a key determinant in their retention efficiency.[17,18] Due to the enhanced permeation and retention (EPR) effect, large-sized nanoparticles inevitably accumulate at untargeted sites in the lungs and other RESs, which poses challenges for the accurate diagnosis of a lung tumor, but opens up the possibility of lung targeting.[19] On the other hand, small-sized nanoparticles exhibit better penetration efficiency, but much weaker accumulation at the target sites due to their rapid circulating metabolism, which is not conducive to imaging and therapeutic purposes.[20,21] For fixed-size nanoprobes, it is a dilemma to strike a balance between targeted retention and efficient penetration.[22,23] Consequently, it is imperative to design size-switchable smart nanoprobes to achieve both deep penetration and long-term retention at the lesion site.

Precise treatment guided by diagnostic information represents a more practical approach. Conventional drug delivery systems may lead to issues such as drug leakage and overload.[24] On-demand activated therapies offer a more promising alternative, in which the cytotoxicity of the therapeutic agent is turned on specifically at the site of lesion. Chemodynamic therapy (CDT) is an emerging cancer treatment with high selectivity, minimal invasion, and few side effects. Catalyzed by metal ions (Mn^{2+}, $Cu^{+/2+}$, Ni^{2+}, Co^{2+}, *etc.*), CDT relies on the Fenton or Fenton-like reaction to decompose H_2O_2 into toxic $^{\bullet}OH$, which disrupts the redox balance of the cells and inhibits tumor cell growth and metastasis.[25–28] The mild acidity and overexpression of H_2O_2 in the TME can be employed as endogenous activation reagents of CDT, offering the possibility of on-demand therapy.[29,30] However, the TME also contains a high concentration of reduced glutathione (GSH), which neutralizes the generated $^{\bullet}OH$ and maintains cellular redox homeostasis, thus affecting CDT efficiency.[31–33] Introducing a GSH depletion mechanism can enhance $^{\bullet}OH$ generation, thereby improving the effectiveness of CDT.[34,35] Therefore, the integration of on-demand activation and enhanced CDT properties into a single theranostic nanoprobe holds significant promise for efficient and minimally toxic therapy.

Herein, we report an innovative design of a size-switchable dual-emissive PLNP-based theranostic nanoprobe ZGMC@ZGC-TAT for ratiometric imaging and on-demand enhanced CDT in response to TME stimulation. We first synthesized acid-degradable green luminescent Mn/Cu co-doped nanorods Zn_2GeO_4:Mn/Cu (ZGMC), which exhibited a harmonious combination of robust pH-responsive afterglow performance and high CDT efficiency. Ultra-small red-emitting nanoparticles $ZnGa_2O_4$:Cr (ZGC) were prepared as the reference and imaging probe. The dual-emissive nanoprobe ZGMC@ZGC-TAT was then constructed by the chemical bonding of two PLNPs, and further bioconjugated with a cell-penetrating peptide (TAT) to improve its cellular uptake efficiency and endow it with biogenic nucleation-fixation-killing properties. Eventually, the prepared TME-stimulated self-regulated ZGMC@ZGC-TAT exhibited exogenous interference-free lung cancer-specific ratiometric signals and showed on-demand enhanced CDT effects. In the simulated TME, its phosphorescence ratio embodied a substantial 214.70 ± 3.74-fold alteration compared to the simulated normal tissues, and the released Cu^{2+} efficiently scavenged GSH and transformed into Cu^{+}, synergizing with the released Mn^{2+} to show potent $^{\bullet}OH$ generation capacity. Precise ratiometric imaging and imaging-guided lung tumor-targeting therapy were achieved *in vivo*. Therefore, ZGMC@ZGC-TAT is regarded as an ideal candidate for precise diagnosis and treatment of lung cancer.

Results and discussion

Design and fabrication of the intelligent theranostic nanoprobe ZGMC@ZGC-TAT

The design strategy and fabrication of ZGMC@ZGC-TAT for lung tumor-specific ratiometric imaging and on-demand enhanced CDT are shown in Fig. 1. ZGMC and ZGC with emission peaks at 537 nm and 700 nm, respectively, were first prepared. Acid-degradable ZGMC was synthesized by a hydrothermal method, and the type and doping amount of luminescence centers were systematically regulated to ensure excellent green phosphorescence emission and efficient CDT effects. For further assembly, ZGMC was sulfhydryl-functionalized with silanization reagents to obtain sulfhydryl-functionalized ZGMC (ZGMC-SH). Simultaneously, ultra-small maleimide-coated red-emitting ZGC-Mal was prepared by thermal decomposition and used as a reference probe. The dual-emissive probe ZGMC@ZGC was then constructed through the coupling reaction between ZGMC-SH and ZGC-Mal.[36] To improve tumor cellular uptake and induce nuclear consolidation, TAT was finally introduced to obtain ZGMC@ZGC-TAT with high tumor specificity and strong therapy effects. The as-prepared ZGMC@ZGC-TAT has a constant luminescence ratio and structural stability under normal physiological conditions, but will automatically decompose under the mildly acidic stimulation of the TME, resulting in a change of luminescence ratio as well as the release of Mn^{2+} and Cu^{2+}. Cu^{2+} consumes

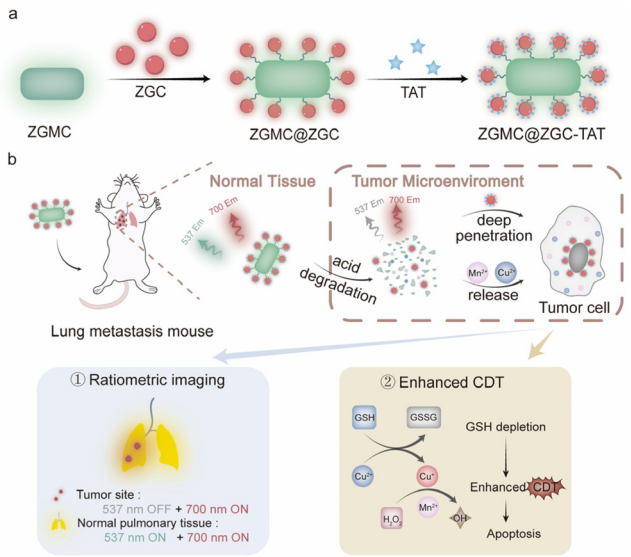

Fig. 1 Illustration of (a) the design strategy and fabrication of ZGMC@ZGC-TAT. (b) The self-evolving nanoprobe ZGMC@ZGC-TAT for lung tumor-targeted ratiometric imaging and on-demand enhanced CDT in response to TME stimulation.

the overexpressed GSH in the TME and further acts as a Fenton-like reaction catalyst together with Mn^{2+} to produce toxic $^{\bullet}OH$ from endogenous H_2O_2, achieving enhanced CDT efficacy. Besides, the degradation product ZGC-TAT can target the nucleus and further cause nuclear pyknosis. Thus, the developed self-evolving nanoprobe ZGMC@ZGC-TAT enables precise TME-stimulated ratiometric imaging along with enhanced on-demand CDT effectiveness.

Preparation and characterization of ZGMC@ZGC-TAT

The green-emitting nanorod ZGMC was first prepared by optimizing the luminescence center doping elements in terms of type and content. In the process of optimization, the crystal structures were consistent with that of Zn_2GeO_4 (JCPDS 11-0687) (Fig. S1a†). However, undesirable changes were observed in the morphological structure while the initial rod-shaped morphology gradually became irregular as the Cu^{2+} doping increased (Fig. S1b–f†). Phosphorescence spectra and afterglow results indicated a negative correlation between the doping amount and both the persistent luminescence (PL) intensity and lifetime (Fig. S2†), and the content of Mn^{2+} was compromised by the Cu^{2+} doping amount as well (Table S1†). Finally, the selected ZGMC with outstanding PL properties and the highest amount of doped Mn^{2+}/Cu^{2+} was synthesized by a hydrothermal method according to the optimized doping amount ($n(Ge^{2+}) : n(Mn^{2+}) : n(Cu^{2+}) = 1 : 0.01 : 0.002$). ZGMC-SH was then prepared and confirmed by the appearance of the stretching vibration of $-CH_2-$ at *ca.* 2920 cm^{-1} and Si–O at 1150 cm^{-1} in the Fourier transform infrared (FT-IR) spectrum (Fig. S3a†). The increase in the concomitant hydrodynamic diameter, accompanied by the zeta potential change, also validated the effective synthesis process (Fig. 2a and b).

Ultra-small spherical red-emitting ZGC was synthesized through the thermal decomposition method, and maleimide-modified for chemical bonding with ZGMC-SH, resulting in the formation of the intermediate product ZGMC@ZGC. The emergence of C=O at 1730 cm^{-1}, –CONH– at 1640 cm^{-1}, and C–O–C at 1110 cm^{-1} was attributed to the successful preparation of ZGMC@ZGC (Fig. S3b and S3c†). The final ZGMC@ZGC-TAT was prepared through further bioconjugation with TAT. The FT-IR spectrum revealed absorption peaks at 3400 cm^{-1} originating from –NH–, verifying the preparation of ZGMC@ZGC-TAT (Fig. S3c†). Additionally, the strong hydrophilicity and electropositivity of TAT led to noticeable increases in the hydrodynamic diameter and zeta potential (Fig. 2a and b). Apart from these, a uniform core–shell configuration with rod-shaped ZGMC as the core and attached granular ZGC was observed, and ZGMC@ZGC-TAT was found to possess a combined spinel phase of both Zn_2GeO_4 and $ZnGa_2O_4$ (Fig. 2c and d). These results comprehensively substantiated the effective preparation of ZGMC@ZGC-TAT, which had consistent morphology and crystal phase throughout the preparation process. Moreover, the prepared ZGMC@ZGC-TAT presented eminent stability in water and phosphate-buffered saline (PBS) with 10% fetal bovine serum (FBS) environments, as proved by marginal variations in XRD patterns (Fig. 2d), hydrodynamic sizes, zeta potentials (Fig. S4†) and FT-IR spectrum (Fig. S5†) over 12 days.

Luminescence properties of ZGMC@ZGC-TAT

The prepared ZGMC@ZGC-TAT featured dual rechargeable emission peaks at both 537 nm and 700 nm, arising from the $^4T_1$ (4G)–$^6A_1$ (6S) transition of Mn^{2+} and Cu^{2+} and the $^2E \rightarrow {}^4A_2$ transition of distorted Cr^{3+}, respectively (Fig. 2e and f). In addition, both PL peaks can also be excited using a 650 nm LED, ensuring the possibility of *in vivo* imaging (Fig. S6†). To study the self-calibration reading nature of ZGMC@ZGC-TAT, its luminescence performance under various simulated physiological testing conditions was investigated, including concentration, voltage and detection time window. The PL ratio of the two emission peaks (I_{700}/I_{537}) considerably remained stable given that the PL of both emission peaks altered synchronously with the increase of the concentration of the nanoprobe and the voltage of the testing apparatus (Fig. 2g, h and S7†). Similarly, the ratio of the afterglow intensity of the two emission peaks remained constant, independent of the detection time (Fig. 2i). All the above results show that the developed nanoprobe ZGMC@ZGC-TAT was capable of counteracting the effects from exogenous factors such as nanoprobe concentration, apparatus conditions, and time gating. Thus, the dual-emissive ZGMC@ZGC-TAT with autofluorescence- and external influence-free renewable luminescence characteristics was expected to achieve precise imaging in a complex matrix.

The pH responsiveness of the ZGMC@ZGC-TAT nanoprobe was subsequently studied. The PL of the emission peak at 537 nm gradually decreased under acidic conditions (pH 6.5 or pH 6.0), while that at 700 nm was unaffected (Fig. 2j and S8a†). As a result, I_{700}/I_{537} increased over time, eventually

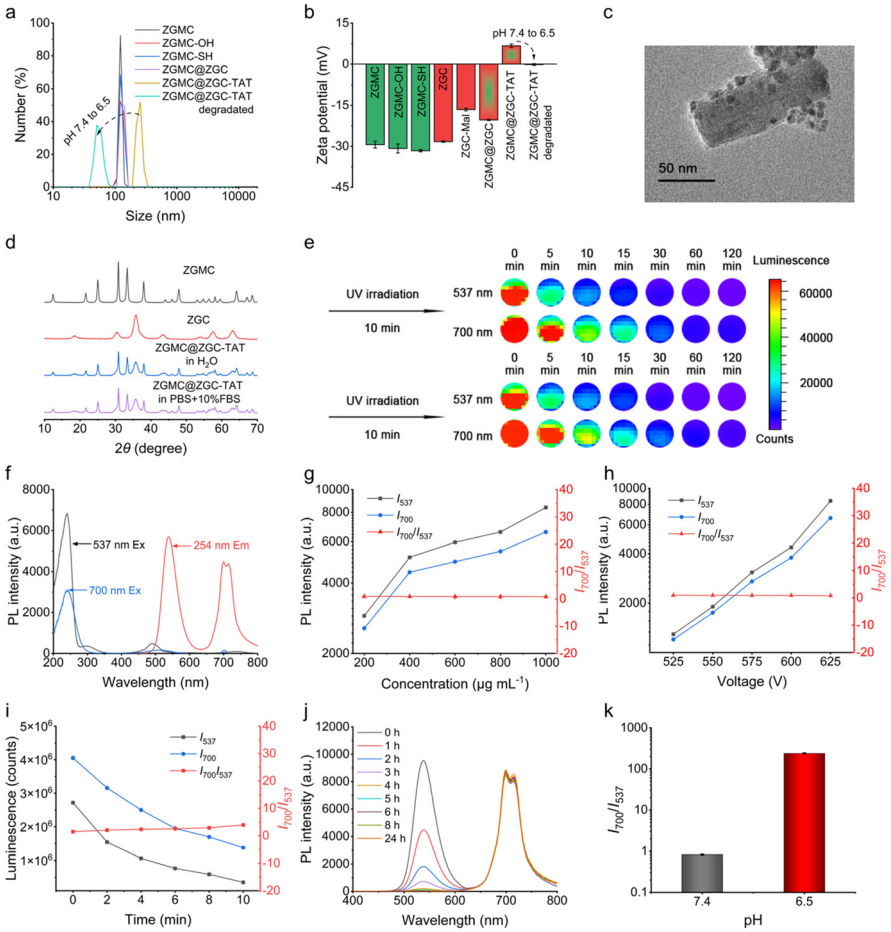

Fig. 2 (a) Hydrated particle size of ZGMC, ZGMC-OH, ZGMC-SH, ZGMC@ZGC, ZGMC@ZGC-TAT, and degraded ZGMC@ZGC-TAT. (b) Zeta potential of ZGMC, ZGMC-OH, ZGMC-SH, ZGC, ZGC-Mal, ZGMC@ZGC, ZGMC@ZGC-TAT, and degraded ZGMC@ZGC-TAT. (c) TEM image of ZGMC@ZGC-TAT. (d) XRD patterns of ZGMC, ZGC, and ZGMC@ZGC-TAT in H_2O and PBS + 10% FBS, respectively. (e) PL images of ZGMC@ZGC-TAT recorded on a Lumina III imaging system. ZGMC@ZGC-TAT was irradiated and re-activated with 254 nm UV irradiation for 10 min before imaging. (f) Excitation (emission at 537 and 700 nm) and emission (excitation at 254 nm) spectra of ZGMC@ZGC-TAT. (g) Effect of concentration of ZGMC@ZGC-TAT on the PL ratio (I_{700}/I_{537}) and the PL intensity at both 537 and 700 nm. (h) Effect of voltage on the PL ratio (I_{700}/I_{537}) and the PL intensity at both 537 and 700 nm of ZGMC@ZGC-TAT. (i) Effect of test time on the luminescence ratio (I_{700}/I_{537}) and the luminescence intensity (537 and 700 nm) of ZGMC@ZGC-TAT recorded on an IVIS Lumina III imaging system. (j) Time-dependent PL spectral changes of ZGMC@ZGC-TAT at pH 6.5. (k) PL ratio (I_{700}/I_{537}) of ZGMC@ZGC-TAT (600 μg mL^{-1}) at pH 7.4 and 6.5.

reaching 273.92 ± 8.05 after 24 hours, far exceeding that in alkaline solutions (0.83 ± 0.02, pH 7.4), which aligned with the unique acid-sensitive nature of green-emitting ZGMC (Fig. 2k and Fig. S8 and S9†). Afterglow image results also demonstrated both the decrease of PL at 537 nm and the constant nature of PL at 700 nm after cessation of excitation light (Fig. S10 and S11†). The PL ratio was significantly enhanced under acidic conditions compared to that under alkaline conditions, making the nanoprobe promising for subsequent *in vivo* specific imaging. In addition, the nanoprobe gradually decomposed from its rod-like core–shell structure to monodispersed ultra-small hyper-spherical particles, leading to a considerable size decrease (Fig. S12†). The sudden reductions in hydrodynamic size and zeta potential further indicated the acid-stimulated size shrinkage (Fig. 2a and b), facilitating the deep penetration and rapid clearance of the nanoprobe into tumor cells. Therefore, ZGMC@ZGC-TAT showed rewarding acid-degradable properties, of which the PL ratio I_{700}/I_{537} varied significantly under different pH conditions. The simultaneous size variation under acidic conditions guaranteed the deep penetration capability of ZGMC@ZGC-TAT, which also bolstered the feasibility of TME-specific ratiometric imaging.

In vitro CDT performance of ZGMC@ZGC-TAT

To verify the acid-activated CDT properties of ZGMC@ZGC-TAT, the release of Mn^{2+} and Cu^{2+} under acidic conditions was analyzed by inductively coupled plasma-mass spectrometry (ICP-MS). The content of Mn^{2+} and Cu^{2+} maximized to 80% at 8 h, and the ion release rate reached 80–90% at 6 h (Fig. 3a and b). The release efficiency of both Mn^{2+} and Cu^{2+} was consistent with the trend and rate of acid degradation of ZGMC@ZGC-TAT. In contrast, no significant release

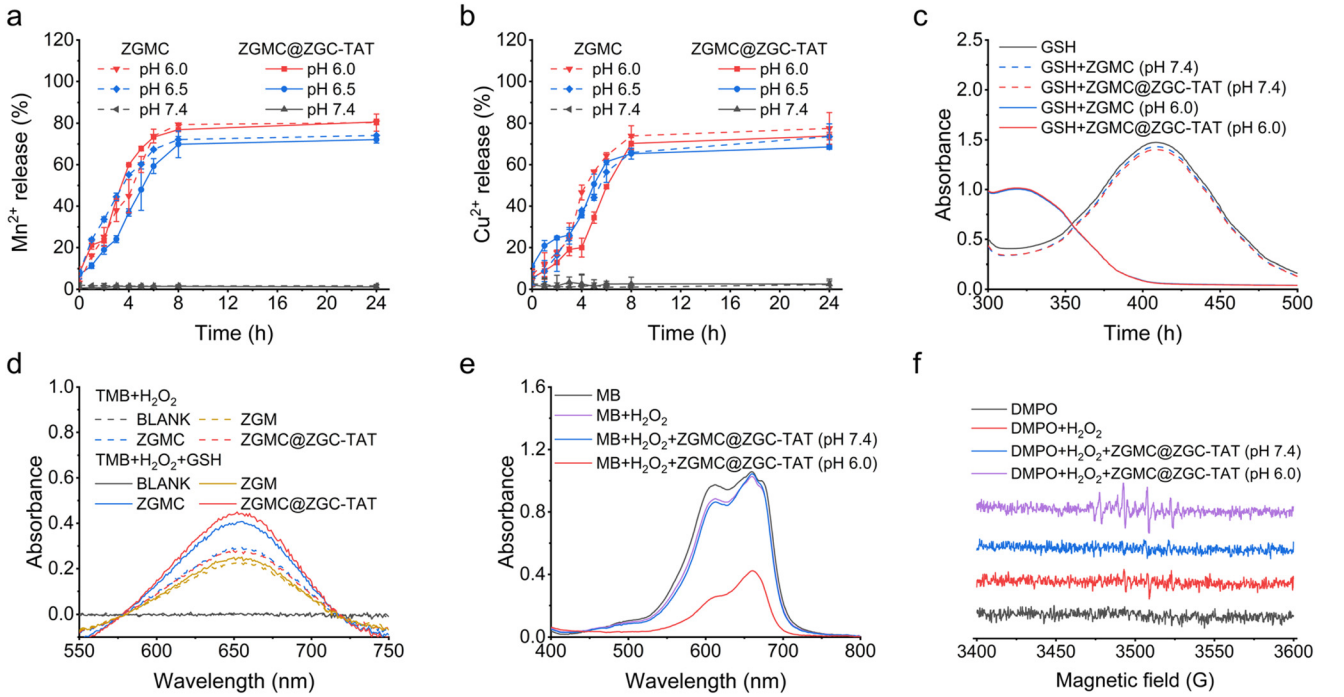

Fig. 3 (a) Time-dependent Mn^{2+} release curves of ZGMC and ZGMC@ZGC-TAT at different pH values. (b) Time-dependent Cu^{2+} release curves of ZGMC and ZGMC@ZGC-TAT at different pH values. (c) UV–vis spectra of different DTNB solutions. (d) UV–vis spectra of different TMB solutions. (e) UV–vis–NIR absorption spectra of different MB solutions. (f) ESR images of different DMPO with or without ZGMC@ZGC-TAT under different conditions.

of metal ions was observed at pH 7.4. It was proved that CDT catalysts can only be released specifically in acid environments, which provided the possibility for subsequent on-demand therapy. Besides, 6 h was selected as a point time for the follow-up studies since the acid degradation of ZGMC@ZGC-TAT peaked at 6 h.

GSH maintains the redox homeostasis in the TME and has a certain inhibitory effect on CDT. The consumption of GSH by ZGMC@ZGC-TAT was then evaluated using the Ellman assay, where the clear 5,5′-dithiobis-2-nitrobenzoic acid (DTNB) was reduced by GSH into yellow 2-nitro-5-mercaptobenzoic acid with an absorbance peak at 410 nm.[37] After 6 h co-incubation of GSH with ZGMC or ZGMC@ZGC-TAT at different pH values, considerable absorbance changes at 410 nm only occurred at pH 6.0, indicating successful depletion of GSH caused by released Cu^{2+} under acidic conditions (Fig. 3c). The absorbance of the above solution gradually decreased with the incubation time (Fig. S13†), implying a satisfactory acid-activated GSH depletion and an effective mechanism to improve antitumor efficiency.

The enhanced CDT effect of ZGMC@ZGC-TAT was further studied in the simulated TME (the acid environment with 10 mmol L^{-1} of H_2O_2 and 10 mmol L^{-1} of GSH), while ZGMC and Zn_2GeO_4:Mn (ZGM) were selected as controls. The indicator TMB exhibited an enhancement of the absorbance at 652 nm during the $^{\bullet}OH$-stimulated transition to oxTMB. In the ZGMC@ZGC-TAT and ZGMC groups, obvious spectral gaps were observed due to the presence of GSH. This is because Cu^{2+} had already been reduced to Cu^{+} by GSH and further reacted with H_2O_2 to generate $^{\bullet}OH$, which promotes the oxidation of TMB. However, GSH had no significant effect on the ZGM-induced TMB oxidation efficiency, thus confirming the indispensable role of Cu^{2+} in improving the CDT efficiency (Fig. 3d). In addition, no significant change in the absorbance was observed under alkaline conditions, meaning that little $^{\bullet}OH$ was produced, indicating the necessity for the coexistence of H_2O_2 and an acid environment (Fig. 3e and S14†). In order to further substantiate the correlation with $^{\bullet}OH$, electron spin resonance (ESR) spectroscopic analysis was conducted with DMPO as the $^{\bullet}OH$ trapping agent. The appearance of DMPO–$^{\bullet}OH$ confirmed the production of $^{\bullet}OH$ (Fig. 3f). In summary, ZGMC@ZGC-TAT can serve as an on-demand Fenton-like reaction catalyst exclusively in acid environments, and simultaneously scavenge endogenous antioxidant GSH overexpressed in the TME, ultimately enhancing the CDT efficiency. Besides, ZGMC@ZGC-TAT has also revealed favorable TME-activated cytotoxicity, which can effectively reduce side effects.

Cell ratiometric imaging and CDT effect of ZGMC@ZGC-TAT

Encouraged by the TME-responsive PL changes and excellent $^{\bullet}OH$ generation ability of ZGMC@ZGC-TAT, cell-targeted imaging and CDT effects were then investigated with model cells (SCC-7 tumor cells cultured in simulated acidic TME and 3T3 normal cells cultured in an alkaline microenvironment). First, with the purpose of studying the TME-responsive cell

internalization and luminescence ratiometric imaging performance, 100 μg mL^{-1} of ZGMC@ZGC-TAT was incubated with SCC-7 cells (pH 6.0) and 3T3 cells (pH 7.4), separately. As shown in Fig. 4a, the imaging results of the SCC-7 cell group showed that green luminescence (I_{537}) slowly faded with the incubation time due to the degradation of ZGMC, the signal donor. At the same time, red-light-signal donors were internalized and gradually accumulated in the cell, accompanied by signal enhancement, which is related to the reduction of the material size and the improvement of penetration. This also resulted in a continuous increase in the signal ratio (I_{700}/I_{537}), reaching a maximum at 10 h. In contrast, both green and red luminescence signals of 3T3 cells remained stable, and the signal ratio of the two channels was significantly different from that of SCC-7 cells (Fig. 4c). These differences are due to pH-stimulated acid degradation and changes in the size of the nanoprobe, also suggesting that the microenvironment can trigger the cell uptake and targeting of ZGMC@ZGC-TAT towards tumor cells.

The TME-triggered CDT effect of ZGMC@ZGC-TAT was then evaluated towards 3T3 and SCC-7 cells *via* the MTT assay. For this purpose, the cells were treated with different concentrations of ZGMC@ZGC-TAT, respectively. When only 50 μg mL^{-1} ZGMC@ZGC-TAT was added, the cell viability of SCC-7 cells at pH 6.0 decreased to 41.03%, and even dropped down to 20.34% at 300 μg mL^{-1} (Fig. 4c). In contrast, the dark cytotoxicity toward 3T3 was negligible and the cell viability remained over 80% even when treated with the highest concentration of ZGMC@ZGC-TAT. Similar results were found in the calcein-AM/PI staining results, where red cell-death signals were only spotted in the SCC-7 cell group cultured in an acidic medium mixed with ZGMC@ZGC-TAT (Fig. S15†). Furthermore, intracellular $^{\bullet}OH$ was evaluated with 2,7-dichlorodihydrofluorescein diacetate (DCFH-DA) as a dictator. DCFH-DA will be hydrolyzed and further oxidized to 2′,7′-dichlorofluorescein by $^{\bullet}OH$ after entering the cell membrane, leading to green fluorescence emission. Obvious green fluorescence signals were observed in SCC-7 cells treated with ZGMC@ZGC-TAT in an acidic environment (pH 6.0), verifying the presence of endogenous H_2O_2 and the reliable generation of cytotoxic $^{\bullet}OH$ (Fig. 4d). All these outcomes confirmed the acid-stimulated and H_2O_2-triggered cellular inhibitory impact and tumor-specific suppression potential of ZGMC@ZGC-TAT, which had delightful prospects for *in vivo* applications.

In vivo pulmonary metastatic tumor imaging and therapy of ZGMC@ZGC-TAT

Given the excellent pH responsiveness, cellular uptake, and tumor cytotoxicity, *in vivo* lung tumor-specific ratiometric imaging and therapy using ZGMC@ZGC-TAT was then investi-

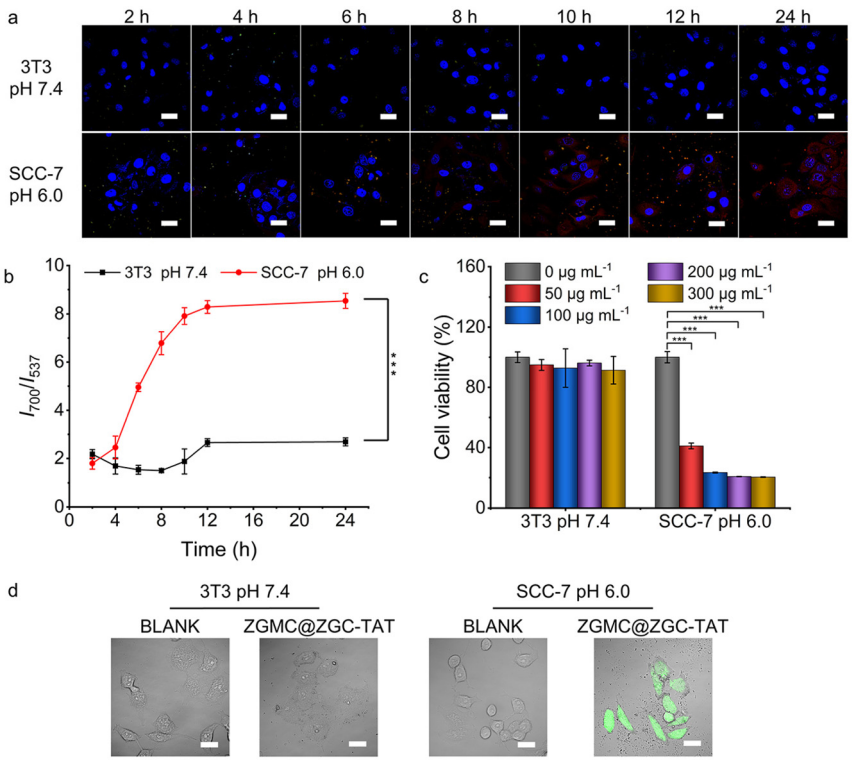

Fig. 4 (a) Cellular internalization and ratiometric imaging of ZGMC@ZGC-TAT toward different cells for different incubation times (scale bar, 30 μm). (b) Luminescence intensity of ZGMC@ZGC-TAT incubated with 3T3 cells at pH 7.4 and with SCC-7 cells at pH 6.0 for different times. ***P < 0.01. (c) Cell viability against 3T3 and SCC-7 cells under different concentrations of ZGMC@ZGC-TAT. Data were presented as the mean ± SD (n = 5). ***P < 0.01. (d) $^{\bullet}OH$ production of 3T3 and SCC-7 cells mediated by ZGMC@ZGC-TAT (300 μg mL^{-1}) as indicated by the fluorescence of DCFH-DA (scale bar, 30 μm).

gated. All animal procedures were performed in accordance with the Guidelines for Care and Use of Laboratory Animals of Jiangnan University and approved by the Animal Ethics Committee of Jiangnan University, People's Republic of China (JN. no 20230530b0300831[246]). The biosafety of ZGMC@ZGC-TAT was first evaluated *via* the hemolysis assay. The hemolysis rate of red blood cells remained under 0.5% after co-incubation with all testing concentrations of ZGMC@ZGC-TAT (Fig S16†), demonstrating trustable biocompatibility of ZGMC@ZGC-TAT for subsequent investigation.

Before investigating the specific imaging of ZGMC@ZGC-TAT for pulmonary metastatic tumors, the ratio imaging effect under the trigger of a subcutaneous tumor microenvironment was first studied. To this end, SCC-7 tumor xenograft mouse models were established, and then an equal amount of ZGMC@ZGC-TAT was injected into the tumor tissues and the corresponding normal tissues when the tumor diameter reached 6 mm. The PL intensity of the green channel at 537 nm declined gradually in tumor tissue exclusively, and little remarkable change in PL intensity in the red channel was observed. Different from normal tissue, a significant increase in the PL ratio I_{700}/I_{537} was observed at the tumor site, reaching its maximum at 10 h post-injection (Fig. S17†). This result indicated that ZGMC@ZGC-TAT also has tumor microenvironment-responsive ratiometric imaging properties *in vivo*, making it possible to effectively distinguish tumor from normal tissue.

The effectiveness of ZGMC@ZGC-TAT in accurate imaging and treatment of pulmonary metastatic tumors was subsequently evaluated. A mouse model with pulmonary metastatic tumors (lung metastasis (+)) was established through an intravenous injection of mouse breast tumor 4T1 cells. The lung CT results showed that in comparison to the left lung, more and larger pulmonary masses were observed in the right lung, and the irregular margins and poor definition of the masses were also more indicative of the spread of malignant tumors in the right lung. *Ex vivo* photographs and H&E staining results also corroborated the cancerous infection situations in both lungs (Fig. 5a and b). ZGMC@ZGC-TAT was injected into lung metastases (+) mice *via* the tail vain, with mouse models without lung metastasis (lung metastases (−)) as the control group. As depicted in Fig. 5c, ZGMC@ZGC-TAT targeted lung tissue and emitted green and red PL signals. The degree of the green PL signal of the cancerous right lung decreased over time, while that of the red PL signal increased slightly, resulting in a notable change in the PL ratio I_{700}/I_{537} ($(I_{700}/I_{500})_{\text{right lung}}$). Besides, $(I_{700}/I_{500})_{\text{right lung}}$ was significantly different from the PL ratio of the left lung ($(I_{700}/I_{500})_{\text{left lung}}$), which is basically constant (Fig. S18†). This phenomenon can be attributed to the multiple synergies of EPR effects, TME-triggered acid degradation, size modulation and the nuclear targeting of TAT. Conversely, the PL signals of the two channels exhibited negligible alterations in the lung metastasis (−) group, with I_{700}/I_{500} remaining stable in both the right and left lungs (Fig. S19 and S20†). All results verified that ZGMC@ZGC-TAT was competent for precise imaging of pulmonary metastatic tumors.

Encouraged by the satisfactory *in vivo* imaging results, the therapeutic effect of ZGMC@ZGC-TAT was then investigated. During the 12-day period, the anatomical lungs of the untreated group presented obvious lesions, the color changed from light pink to dark red, and more and more pulmonary metastatic nodules could be observed on the surface. In contrast, the nodule growth in the group treated with ZGMC@ZGC-TAT was suppressed (Fig. 6a). At the end of treatment, the number of pulmonary metastatic nodules in the untreated group was significantly higher than that in the ZGMC@ZGC-TAT group, which confirmed that ZGMC@ZGC-TAT had a good inhibitory effect on pulmonary metastatic tumors. This is also demonstrated by the increase in the lung weight caused by tumor proliferation (Fig. 6b and c). In addition, the weight loss of untreated mice also confirmed the alleviation of the degree of lung metastasis by ZGMC@ZGC-TAT because lung tumors cause wasting in mice (Fig. 6d). It is worth mentioning that the body weight of mice in the ZGMC@ZGC-TAT group did not decrease significantly. The main organs were not significantly damaged as proved by H&E staining (Fig. 6e) and all blood indicators were within the

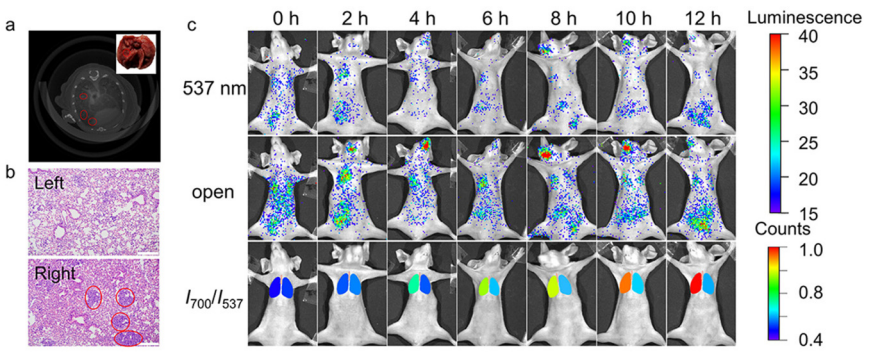

Fig. 5 (a) CT image and *ex vivo* photograph (inset) of lung metastasis (+) mouse models. (b) H&E staining of the left and right lungs (scale bar, 200 μm). The locations of tumors are marked by the red circles. (c) *In vivo* luminescence images of lung metastasis (+) mouse models after being intravenously injected with ZGMC@ZGC-TAT over time.

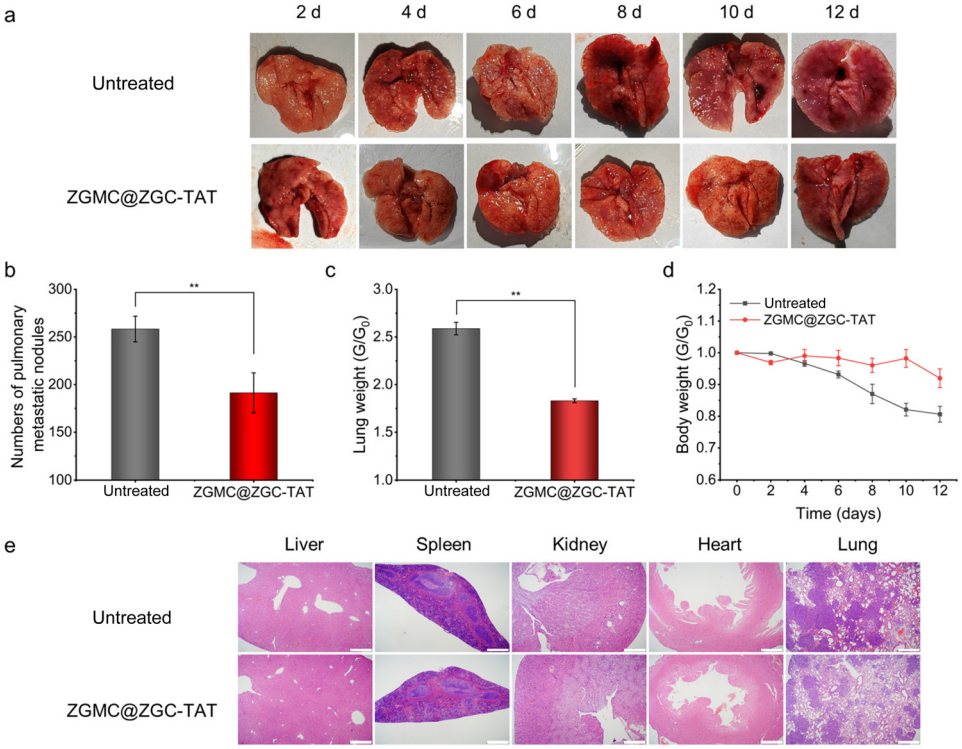

Fig. 6 (a) Photographs of the lungs from lung metastasis (+) mouse models after different treatments for different times. (b) A number of pulmonary metastatic nodules of lung metastasis (+) mouse models after different treatments. (c) The relative lung weight of lung metastasis (+) mouse models after different treatments. (d) The relative body weight of lung metastasis (+) mouse models after different treatments over time. (e) H&E staining of major organs and lung tissue in lung metastasis (+) mouse models (scale bar, 500 μm).

normal limits (Fig. S21†), indicating that the biological toxicity of ZGMC@ZGC-TAT was negligible. Therefore, ZGMC@ZGC-TAT can effectively reduce the formation of pulmonary metastatic nodules and thus serve to inhibit lung metastasis with fewer side effects. All of the above results confirmed that ZGMC@ZGC-TAT was equipped with *in vivo* TME-responsive ratiometric imaging, on-demand tumor suppressive performance and negligible biotoxicity, which make it highly promising for precise pulmonary metastatic tumor theranostics.

Conclusions

In summary, motivated by the non-target retention of PLNPs in the lungs, we here report a pH-responsive dual-emissive self-evolving PLNP-based theranostic nanoprobe ZGMC@ZGC-TAT for autofluorescence-free ratiometric imaging and on-demand enhanced CDT of pulmonary metastasis. The developed nanoprobe emits two luminescence peaks at 537 nm and 700 nm with an acid-sensitive luminescence ratio signal of I_{700}/I_{500}, which endows it with *in situ* excitation- and external disturbance-free and TME-responsive PL ratiometric imaging capabilities. The corresponding pH-triggered size self-adjustment further strengthened the tumor-active targeting and TME-specific imaging for xenograft tumor and pulmonary metastasis. Simultaneously, ZGMC@ZGC-TAT is characterized by enhanced CDT efficiency owing to TME-triggered GSH depletion. The satisfactory bio-compatibility and CDT-based antitumor capacity with negligible side effects of ZGMC@ZGC-TAT further indicated the great potential for accurate TME-specific imaging-guided metastasis suppression. We believe that the developed microenvironment-responsive and size-switchable dual-emissive PLNP-based intelligent theranostic nanoprobe ZGMC@ZGC-TAT provides a novel perspective on accurate pulmonary cancer imaging with on-demand therapy, and positively impacts the designs of *in vivo* responsive probes.

Author contributions

Xu Zhao: conceptualization, methodology, validation, supervision, funding acquisition, and writing – review & editing. Tian-Yue Gu: conceptualization, investigation, validation, methodology, data curation, formal analysis, and writing – original draft. You-Peng Xia and Xue-Mei Gao: investigation and validation. Li-Jian Chen and Li-Xia Yan: methodology and investigation. Xiu-Ping Yan: conceptualization, supervision, funding

acquisition, and writing – review & editing. All authors have read and approved the final manuscript.

Conflicts of interest

There are no conflicts to declare.

Acknowledgements

This work was supported by the National Natural Science Foundation of China (No. 21934002 and 21804056), the Natural Science Foundation of Jiangsu Province, China (No. BK20231491 and BK20180581) and the Collaborative Innovation Center of Food Safety and Quality Control in Jiangsu Province.

References

1 Z. Wang, Y. Ma, H. Wang, F. Wang, T. Xu and Y. Gu, *Adv. Funct. Mater.*, 2019, **29**, 1905480.
2 Q. Wang, J. Liu, D. Chen, S. Miao, J. Wen, C. Liu, S. Xue, Y. Liu, Q. Zhang and Y. Shen, *Adv. Healthcare Mater.*, 2023, **12**, 2202622.
3 D. R. Welch and D. R. Hurst, *Cancer Res.*, 2019, **79**, 3011–3027.
4 M. Terao and N. Niikura, *Transl. Cancer Res.*, 2020, **9**, 5032–5037.
5 J. Budczies, M. von Winterfeld, F. Klauschen, M. Bockmayr, J. K. Lennerz, C. Denkert, T. Wolf, A. Warth, M. Dietel, I. Anagnostopoulos, W. Weichert, D. Wittschieber and A. Stenzinger, *Oncotarget*, 2014, **6**, 570–583.
6 T. N. Seyfried and L. C. Huysentruyt, *Crit. Rev. Oncog.*, 2013, **18**, 43–73.
7 R. L. Siegel, A. N. Giaquinto and A. Jemal, *CA Cancer J. Clin.*, 2024, **74**, 12–49.
8 Y. Huang, T. Xie, K. Zou, Y. Gu, G. Yang, F. Zhang, L.-L. Qu and S. Yang, *Nanoscale*, 2021, **13**, 13344–13352.
9 J. Hu, D. H. Ortgies, E. Martín Rodríguez, F. Rivero, R. Aguilar Torres, F. Alfonso, N. Fernández, G. Carreño-Tarragona, L. Monge, F. Sanz-Rodriguez, M. del C. Iglesias, M. Granado, A. L. García-Villalon, J. García Solé and D. Jaque, *Adv. Opt. Mater.*, 2018, **6**, 1800626.
10 Y. Jiang and K. Pu, *Chem. Rev.*, 2021, **121**, 13086–13131.
11 A. Grebinyk, O. Chepurna, M. Frohme, J. Qu, R. Patil, L. O. Vretik and T. Y. Ohulchanskyy, *J. Photochem. Photobiol., C*, 2024, **58**, 100652.
12 X. Sun, L. Song, N. Liu, J. Shi and Y. Zhang, *ACS Appl. Nano Mater.*, 2021, **4**, 6497–6514.
13 X. Zhao, X.-M. Gao, T.-Y. Gu, K.-L. Chen, Z.-Y. Yan, L.-J. Chen and X.-P. Yan, *TrAC, Trends Anal. Chem.*, 2023, **168**, 117279.
14 J.-X. Guo, L.-M. Pan, M.-C. Wang, L.-J. Chen and X. Zhao, *Food Chem.*, 2023, **413**, 135611.
15 L.-M. Pan, X. Zhao, X. Wei, L.-J. Chen, C. Wang and X.-P. Yan, *Anal. Chem.*, 2022, **94**, 6387–6393.
16 J.-L. Liu, X. Zhao, L.-J. Chen, L.-M. Pan and X.-P. Yan, *Anal. Chem.*, 2021, **93**, 7348–7354.
17 A. Albanese, P. S. Tang and W. C. W. Chan, *Annu. Rev. Biomed. Eng.*, 2012, **14**, 1–16.
18 J. Wang, M. Zha, H. Zhao, W. Yue, D. Wu and K. Li, *Anal. Chem.*, 2022, **94**, 4005–4011.
19 B. Theek, M. Baues, T. Ojha, D. Möckel, S. K. Veettil, J. Steitz, L. van Bloois, G. Storm, F. Kiessling and T. Lammers, *J. Controlled Release*, 2016, **231**, 77–85.
20 J. Xu, M. Song, Z. Fang, L. Zheng, X. Huang and K. Liu, *J. Controlled Release*, 2023, **353**, 699–712.
21 X. Cun, M. Li, S. Wang, Y. Wang, J. Wang, Z. Lu, R. Yang, X. Tang, Z. Zhang and Q. He, *Nanoscale*, 2018, **10**, 9935–9948.
22 W. Wu, L. Luo, Y. Wang, Q. Wu, H.-B. Dai, J.-S. Li, C. Durkan, N. Wang and G.-X. Wang, *Theranostics*, 2018, **8**, 3038–3058.
23 S. Ruan, X. Cao, X. Cun, G. Hu, Y. Zhou, Y. Zhang, L. Lu, Q. He and H. Gao, *Biomaterials*, 2015, **60**, 100–110.
24 L. Haas, A. Elewaut, C. L. Gerard, C. Umkehrer, L. Leiendecker, M. Pedersen, I. Krecioch, D. Hoffmann, M. Novatchkova, M. Kuttke, T. Neumann, I. P. da Silva, H. Witthock, M. A. Cuendet, S. Carotta, K. J. Harrington, J. Zuber, R. A. Scolyer, G. V. Long, J. S. Wilmott, O. Michielin, S. Vanharanta, T. Wiesner and A. C. Obenauf, *Nat. Cancer*, 2021, **2**, 693–708.
25 S. Gao, Y. Jin, K. Ge, Z. Li, H. Liu, X. Dai, Y. Zhang, S. Chen, X. Liang and J. Zhang, *Adv. Sci.*, 2019, **6**, 1902137.
26 H. Liu, Y. You, Y. Sang, F. Pu, J. Ren and X. Qu, *Chem. – Eur. J.*, 2021, **27**, 18201–18207.
27 R. Yuan, Y. Li, Z. Wang, L. Jia, X. Guo and S. Zhou, *Nano Today*, 2023, **51**, 101899.
28 L. M. Chong, D. J. H. Tng, L. L. Y. Tan, M. L. K. Chua and Y. Zhang, *Appl. Phys. Rev.*, 2021, **8**, 041322.
29 H. S. El-Sawy, A. M. Al-Abd, T. A. Ahmed, K. M. El-Say and V. P. Torchilin, *ACS Nano*, 2018, **12**, 10636–10664.
30 Z. Zhou and Z.-R. Lu, *Adv. Drug Delivery Rev.*, 2017, **113**, 24–48.
31 L. Zhang, C.-X. Li, S.-S. Wan and X.-Z. Zhang, *Adv. Healthcare Mater.*, 2022, **11**, 2101971.
32 Q. Tian, F. Xue, Y. Wang, Y. Cheng, L. An, S. Yang, X. Chen and G. Huang, *Nano Today*, 2021, **39**, 101162.
33 J. Wang, Y.-X. Liu, X.-L. Li, H.-Y. Chen and J.-J. Xu, *Anal. Chem.*, 2021, **93**, 10317–10325.
34 Y. Wang, J. Wang, Y. Jiao, K. Chen, T. Chen, X. Wu, X. Jiang, W. Bu, C. Liu and X. Qu, *Acta Biomater.*, 2023, **172**, 423–440.
35 Y. Huang, S. Wu, L. Zhang, Q. Deng, J. Ren and X. Qu, *ACS Nano*, 2022, **16**, 4228–4238.
36 W. Huang, X. Wu, X. Gao, Y. Yu, H. Lei, Z. Zhu, Y. Shi, Y. Chen, M. Qin, W. Wang and Y. Cao, *Nat. Chem.*, 2019, **11**, 310–319.
37 M. Hou, M. Liu, H. Yu, Y. Kou, J. Jia, Q. Zhou, F. Zhang, D. Zhao, T. Zhao and X. Li, *Nano Lett.*, 2024, **24**, 1284–1293.